Zhang *et al. Chem Synth* 2024;4:21
DOI: 10.20517/cs.2023.65

Chemical Synthesis

Research Article

Open Access

Construction of piezoelectric photocatalyst Au/$BiVO_4$ for efficient degradation of tetracycline and studied at single-particle level

Yujia Zhang[1], Yan Liu[2], Xueqin Gong[1], Zeyan Wang[1], Yuanyuan Liu[1], Peng Wang[1], Hefeng Cheng[1], Baibiao Huang[1], Zhaoke Zheng[1,*]

[1]State Key Laboratory of Crystal Materials, Shandong University, Jinan 250100, Shandong, China.
[2]Center for Optics Research and Engineering, Shandong University, Qingdao 266237, Shandong, China.

[*]**Correspondence to:** Prof. Zhaoke Zheng, State Key Laboratory of Crystal Materials, Shandong University, 27 Shanda South Road, Jinan 250100, Shandong, China. E-mail: zkzheng@sdu.edu.cn

How to cite this article: Zhang Y, Liu Y, Gong X, Wang Z, Liu Y, Wang P, Cheng H, Huang B, Zheng Z. Construction of piezoelectric photocatalyst Au/$BiVO_4$ for efficient degradation of tetracycline and studied at single-particle level. *Chem Synth* 2024;4:21. https://dx.doi.org/10.20517/cs.2023.65

Received: 19 Dec 2023 **First Decision:** 31 Jan 2024 **Revised:** 26 Feb 2024 **Accepted:** 5 Mar 2024 **Published:** 3 Apr 2024

Academic Editor: Jun Xu **Copy Editor:** Dong-Li Li **Production Editor:** Dong-Li Li

Abstract

Piezopotential-assisted catalysis has been proven to be a low-cost and high-efficiency environmental purification process. Herein, Au/bismuth vanadate ($BiVO_4$) piezoelectric photocatalysts are prepared by modifying highly dispersed Au nanoparticles (AuNPs) on piezoelectric $BiVO_4$ microcrystal by a deposition-precipitation approach. Under visible light irradiation and assisted ultrasound excitation, the removal rate of tetracycline was 95% within 60 min, demonstrating the optimum photocatalytic performance over 3Au/$BiVO_4$. The significantly enhanced photocatalytic performance is due to the synergistic coupling of plasmonic and piezotronic effect based on facet engineering. Single-particle spectroscopy technology can provide photoluminescence (PL) lifetime and PL spectra information in the micro-/nano regions, thereby exploring the charge transfer behavior of heterostructures. Single-particle PL images revealed a significant attenuation of PL emission and shortened PL lifetime of 3Au/$BiVO_4$, compared with $BiVO_4$, indicating that high-density dispersed AuNPs promote charge transfer. In situ monitoring of individual $BiVO_4$ and 3Au/$BiVO_4$ particles before and after polarization treatment confirms that the piezoelectric field of the $BiVO_4$ decahedron further promotes separation of photogenerated carriers induced by plasmonic effect. Driven by the piezoelectric potential induced by ultrasonic vibration near the heterostructures, high-energy hot electrons excited on plasmonic AuNPs can be effectively extracted to $BiVO_4$. This work provides new choices for designing high-performance pollutant treatment catalysts.

Keywords: Piezo-/photocatalytic, surface plasmon resonance, facet engineering, organic pollutant degradation, single-particle study

INTRODUCTION

In recent decades, antibiotic wastewater generated during industrialization has caused serious environmental problems[1]. Among them, tetracycline (TC) is the most common antibiotic to deal with bacterial infections, and it is often discharged into wastewater and soil due to improper disposal[2-4]. Photocatalytic technology is currently one of the most popular methods for treating organic pollutants, microorganisms, and heavy metal ions in wastewater due to its environmentally friendly, efficient, and low-cost characteristics[5-10]. However, the rapid recombination of photogenerated charge carriers remains the main bottleneck of photocatalytic performance[11-14]. Therefore, it is very necessary to enhance the driving force for the internal separation/transmission of photogenerated carriers[15,16].

Integrating the piezoelectric effect into photocatalysts is a promising approach, which not only increases the carrier concentration (sufficient photogenerated electrons and holes) but also promotes the separation of carriers through the internal electric field generated by piezoelectric polarization[17-21]. Piezoelectric polarization refers to the generation of polarized charges with opposite polarity when a piezoelectric material is subjected to external stress, which separate and migrate on the polar surface, thus forming a piezoelectric potential[22-25]. Meanwhile, piezoelectric potential facilitates the separation of electron-hole pairs and generates active species for oxidation-reduction reactions on the material surface, which has great potential for achieving in-situ catalytic degradation of organic pollutants[26-29]. However, due to the limited carrier transport capacity of piezoelectric materials, the piezoelectric catalytic performance was greatly constrained. The surface plasmon resonance (SPR) effect of noble metal nanocrystals can provide new opportunities for improving the piezo-photocatalytic performance. The noble metal nanocrystals have a large work function (i.e., high electronegativity), and when combined with semiconductors, they can promote the transfer of interface electrons and suppress the recombination process of electron-hole interactions[30]. In addition, SPR catalysis has the characteristics of an adjustable light response range[31-35]. So far, several heterostructures coupled with SPR effect and piezoelectric polarization have been studied and applied in the removal of organic wastewater and environmental pollutants. Xu *et al.* reported that $Au_4/BaTiO_3$ completely degraded methyl orange (MO) within 75 min under full spectrum light irradiation and assisted ultrasound excitation[36]. Li *et al.* confirmed that the efficiency of photocatalytic hydrogen production and Rhodamine B (RhB) degradation on $Au/AgNbO_3$ under ultrasound vibration assistance were significantly increased[37].

In recent years, non-centrosymmetric Bi-based piezoelectric materials have been widely used[38,39]. As developed by Xu *et al.*, $Fe^{III}/BiOIO_3$ piezoelectric catalyst achieves efficient piezo-catalytic self-Fenton (PSF)[38]. Among them, the monoclinic bismuth vanadate (m-$BiVO_4$) semiconductor has been widely studied for its visible light response (~2.4 eV), abundant availability, and excellent optoelectronic properties[40-42]. Meanwhile, it has the potential to be used as a piezoelectric catalyst because it is a ferroelectric material, and the crystal facet effect for the decahedral $BiVO_4$ can promote the electrons and holes induced by piezoelectric potential transfer to different facets[43,44]. Wei *et al.* reported that noble metal Au nanoparticles (AuNPs) as electron capture sites enhanced the piezoelectric catalytic activity of $BiVO_4$[45]. However, to our knowledge, there are currently no studies reporting the enhancement of plasmonic photocatalytic activity by piezoelectric polarization in $BiVO_4$. Therefore, our aim is to combine SPR with piezoelectric photocatalysis by modifying highly dispersed AuNPs on decahedral $BiVO_4$ microcrystals and exploiting the coupling of surface energetic hot electrons and piezoelectric effects in hybrid structures to enhance their catalytic performance. Moreover, a few intuitive studies demonstrate that introducing SPR or piezo-phototronic effect can significantly enhance the charge separation and transport capabilities of

heterojunctions. Single-particle photoluminescence (PL) spectroscopy can address this challenge by identifying charge transfer induced by SPR and piezoelectric effects.

Herein, the Au/$BiVO_4$ heterostructure photocatalyst was synthesized by simple hydrothermal and deposition-precipitation methods. Under the action of ultrasound, the induced piezoelectric potential in $BiVO_4$ is beneficial for extracting energetic hot electrons generated on plasmonic AuNPs under visible light, suppressing the recombination of photogenerated electron and hole pairs and significantly improving the photocatalytic degradation of TC and RhB. Single-particle spectroscopy can accurately monitor the SPR effect and piezoelectric field (polarization treatment) enhanced charge separation. Compared with $BiVO_4$, the PL lifetime of 3Au/$BiVO_4$ is shortened, and the average attenuation rate of PL intensity is at least 60%, indicating that high-density dispersed AuNPs promote charge transfer. Similarly, in situ single-particle PL tests were conducted during catalytic degradation of TC before and after polarization treatment. The results showed that the SPR effects (AuNPs) and piezoelectric catalysis of $BiVO_4$ synergistically promoted the photocatalytic activity of Au/$BiVO_4$ heterostructures.

EXPERIMENTAL

Chemicals

Bismuth nitrate pentahydrate [$Bi(NO_3)_3{\cdot}5H_2O$], ammonium metavanadate (NH_4VO_3), nitric acid (HNO_3), ammonia solution (NH_4OH), urea (CH_4N_2O), and Gold chloride trihydrate ($HAuCl_4{\cdot}3H_2O$) were all purchased from Aladdin Chemistry Co., Ltd. These chemicals were used as received without any further purification.

Preparation of Au/$BiVO_4$ heterostructures

The preparation method of decahedral $BiVO_4$ microcrystals is based on our previous work[46]. Highly dispersed xAu/$BiVO_4$ were synthesized by an aqueous heating process with urea as a reducing agent[47]. In the typical synthesis, the as-prepared $BiVO_4$ powder (100 mg) is uniformly dispersed in 20 mL deionized water, sonicated in a water bath for 15 min, followed by 15 min vigorous stirring. Then, add a certain amount (1, 3 or 5 mL) of $HAuCl_4{\cdot}3H_2O$ aqueous solution (1 mg/mL) to the above suspension, ensuring the random deposition of Au on $BiVO_4$. Later, 200 mg urea was introduced into the above solution to fully reduce Au ions, resulting in a bright yellow solution heated at a constant temperature of 80 °C for 3 h. Wash the obtained samples multiple times with deionized water and ethanol and dry them in a 70 °C vacuum drying oven. Finally, the samples were calcined at 400 °C in an Ar atmosphere for 3 h to obtain the highly-deposited Au/$BiVO_4$.

Deposition of single metals/oxides on monoclinic $BiVO_4$

The synthesis details were displayed in the Supplementary Materials.

Characterizations

The characterization details were provided in the Supplementary Materials.

Piezo-/photocatalytic performance measuretures

In the typical process, 20 mg catalyst was suspended in 50 mL TC/RhB aqueous solution (20 $mg{\cdot}L^{-1}$) and magnetically stirred at room temperature. Firstly, magnetically stirring the suspension in the dark for 30 min achieved adsorption-desorption equilibrium. The suspension was then irradiated under a Xe lamp (300 W, CEL-HFX300) equipped with a 420 nm filter and/or ultrasonic cleaner (100 W, 40 kHz). The concentration of TC was measured by ultraviolet-visible (UV-vis) absorption spectra at 357 nm (Cary 5000, the maximum absorption of TC). During the photocatalytic degradation, 4 mL solution was taken out and centrifuged after a certain interval. The temperature of the reaction equipment was kept at 20 °C using cool

water recirculation equipment. Three cyclic experiments were conducted under the same conditions to check the durability of the photocatalyst. After each test, the catalyst was centrifuged, extensively washed with deionized water several times, and dried at 60 °C for the next recycle.

Photoelectrocatalytic measurements

The photoelectrochemical measurements were carried out in 0.1 M potassium phosphate (KPi) buffer solution (pH = 7) by using a three-electrode electrochemical cell, with a Pt wire as counter electrode, saturated Ag/AgCl electrode as a reference electrode, and the catalyst-coated FTO glass (1.0 cm × 1.0 cm) as the working electrode, respectively.

The testing steps for photoelectrocatalytic are detailed in the Supplementary Materials.

Single-particle time-resolved photoluminescence spectroscopy measurement

The quartz cover glasses were ultrasonically cleaned with concentrate nitric acid solution for 20 min, then rinsed continuously with high-purity water for 30 min. Subsequently, the well-dispersed water-soluble sample suspension was dropped onto a clean cover glass for 40 s and spin-coated at 4,000 rpm. Anneal the cover glass covered with the sample at 90 °C for 1 h to fix the particles on the glass surface.

Record the PL intensity and PL lifetime using an objective scanning confocal microscope system (PicoQuant, MicroTime 200) coupled with the Olympus IX73 inverted fluorescence microscope. The data collected by the MultiHarp 150 TCSPC module (PicoQuant) is stored in the time-tagged time-resolved mode. The single-particle spectra were obtained using an electron multiplying charge-coupled device (EMCCD) (Andor, DU970P-BVF) and high-resolution Spectrograph (Andor, Shamrock 500i) coupled with a fiber connector. The acquisition time of single-particle PL spectra is 10 s. The samples were excited by a 405 nm pulsed wave laser. The laser frequency was set to 10 MHz.

RESULTS AND DISCUSSION

The synthesis route of the Au/$BiVO_4$ heterostructures is presented in Figure 1A. Firstly, decahedral $BiVO_4$ were prepared by a simple hydrothermal method. As presented in Supplementary Figure 1, the panoramic scanning electron microscope (SEM) image shows that the individual $BiVO_4$ exhibits a regular decahedral morphology, and the main exposed crystal facets are (010) and (110), which can be proven by the photodeposition experiments that Pt nanoparticles and MnO_2 are reduced and oxidized on the (010) and (110) facets, respectively [Supplementary Figure 1]. Afterward, Au atoms and small nanoparticles were uniformly dispersed on the surface of $BiVO_4$ through a solution phase process. After controlling the calcination process, high-density dispersed Au particles are decorated on the surface of the as-prepared $BiVO_4$ decahedron to obtain the xAu/$BiVO_4$ heterostructure. The samples are named xAu/$BiVO_4$ based on the mass load of Au. The SEM images show that the density of AuNPs in the as-prepared xAu/$BiVO_4$ heterostructure changes significantly with the addition of $HAuCl_4 \cdot 3H_2O$ [Figure 1B-D]. Notably, the size of the AuNPs slightly increases with increased $HAuCl_4 \cdot 3H_2O$ content. This may be due to the higher concentration of added Au, causing a large accumulation of nucleation spots.

As shown in a transmission electron microscopy (TEM) image, AuNPs are homogeneously loaded on decahedral $BiVO_4$ [Figure 1E]. A high-resolution TEM (HRTEM) image displays that both the decahedral $BiVO_4$ and the AuNPs (with an average diameter of 8 nm) have good crystallinity and preferential crystal orientation, forming the 3Au/$BiVO_4$ heterostructure [Figure 1F]. The lattice fringes are measured to be 2.35 Å, which corresponds well to the (111) planes of cubic Au. Due to the influence of the thickness of $BiVO_4$, its lattice fringes are not easily observed. However, the seamless contact between these two crystals

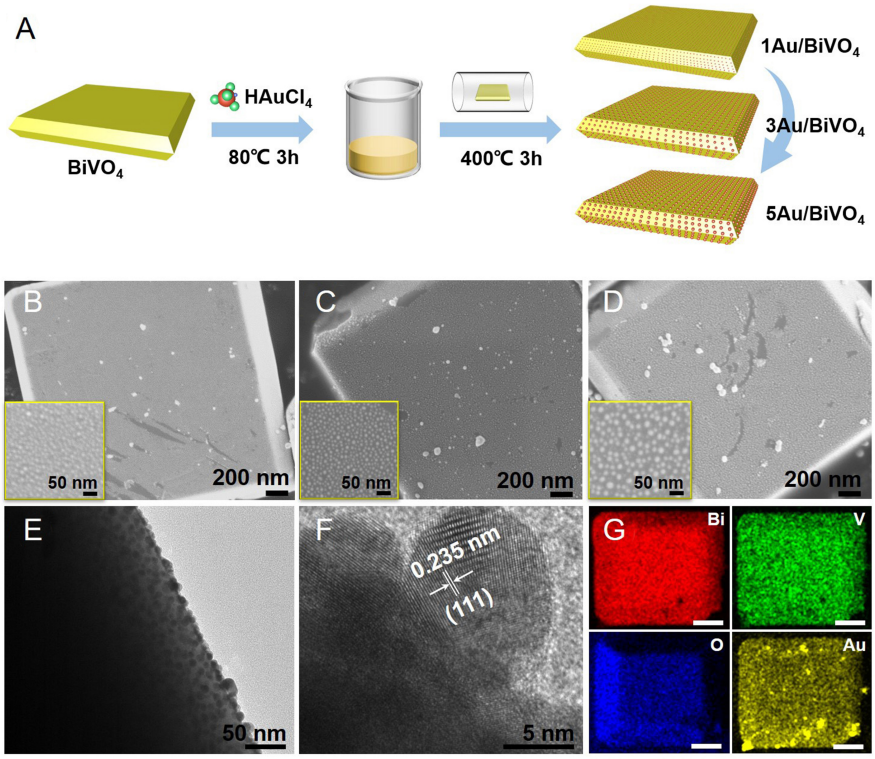

Figure 1. (A) Schematic diagram of the synthesis route of the xAu/$BiVO_4$ heterojunction; (B-D) SEM images of the xAu/$BiVO_4$ heterostructures (x = 1, 3, 5); (E and F) HRTEM images of 3Au/$BiVO_4$; (G) EDS elemental mapping images of the 3Au/$BiVO_4$ heterostructures. The scales in Figure 1G all represent 1 um. $BiVO_4$: Bismuth vanadate; SEM: scanning electron microscope; HRTEM: high-resolution transmission electron microscopy; EDS: energy-dispersive X-ray spectroscopy.

can prove the possibility of electron transfer from AuNPs to the surface of $BiVO_4$. The corresponding energy-dispersive X-ray spectroscopy (EDS) mappings display uniformly distributed Bi, V, O, and Au elements on the 3Au/$BiVO_4$ heterostructure, fce highly dispersed on the decahedral $BiVO_4$ [Figure 1G and Supplementary Figure 2].

The phase structures of the $BiVO_4$ and xAu/$BiVO_4$ heterostructure were analyzed by X-ray diffraction (XRD). The XRD results indicate that the synthesized decahedral $BiVO_4$ belongs to the monoclinic phase (JCPDS NO. 14-0688)[46]. After loading AuNPs, a new peak observed at 38.0° assigned to the (111) facet of cubic phase Au (JCPDS No. 65-2870) demonstrates the formation of xAu/$BiVO_4$ heterostructure [Figure 2A][48]. As presented in Figure 2A, it can be clearly observed that the intensity of the XRD peak for Au (111) facets rises with the increase of added $HAuCl_4 \cdot 3H_2O$ content. The spectral absorption characteristics of $BiVO_4$ and xAu/$BiVO_4$ heterostructures were further measured using UV-vis diffuse reflectance spectroscopy (DRS) [Figure 2B]. The pure $BiVO_4$ exhibits an absorption edge extending to around 545 nm, with a bandgap value of 2.28 eV [Supplementary Figure 3][49]. After loading AuNPs on the decahedral $BiVO_4$, an additional characteristic absorption at ~620 nm is observed, which is due to the SPR induced by AuNPs.

Furthermore, the X-ray photoelectron spectroscopy (XPS) spectra were conducted to measure chemical binding states of xAu/$BiVO_4$. Figure 2C shows the full XPS spectrum, which displays the characteristic peaks of Bi 4f, V 2p, O 1s and Au 4f signals, which is consistent with the EDS mapping measurements. As presented in Figure 2D, the two characteristic peaks observed in the XPS spectrum of Bi 4f at 159.1 and

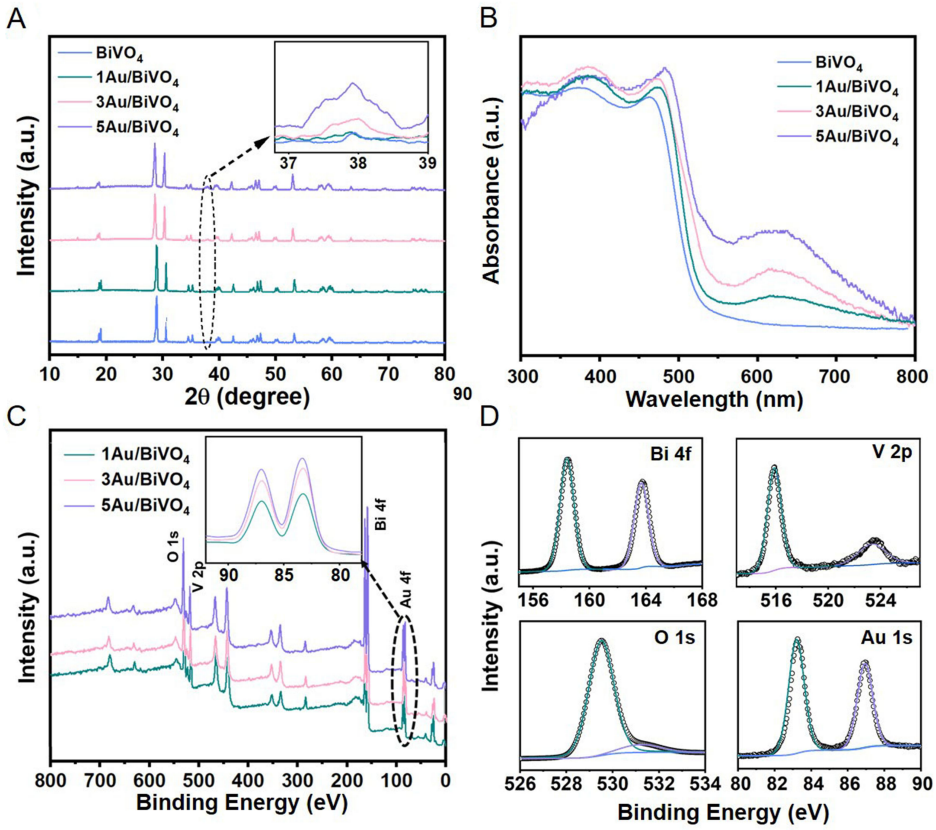

Figure 2. Characterizations of the xAu/$BiVO_4$ heterostructures. (A) XRD patterns; (B) UV-vis DRS test; (C) XPS full spectrum; (D) High-resolution XPS spectra of Bi 4f, V 2p, O 1s, Au 1s over 3Au/$BiVO_4$. $BiVO_4$: Bismuth vanadate; XRD: X-ray diffraction; UV-vis: ultraviolet-visible; DRS: diffuse reflectance spectroscopy; XPS: X-ray photoelectron spectroscopy.

164.4 eV belong to Bi $4f_{7/2}$ and Bi $4f_{5/2}$, respectively, which belong to Bi^{3+} in the lattice[50,51]. The $2p_{1/2}$ and $2p_{3/2}$ peaks are located at 516.4 and 524.1 eV, which is attributed to V^{5+} cation on pure $BiVO_4$ [Figure 2D]. Additionally, O 1s peaks at low-binding energies (BE) (529.5 eV) and high-BE (531.2 eV) are indexed to lattice O (O_L) and adsorbed O (O_A), respectively [Figure 2D]. As shown in Figure 2D, the two characteristic peaks located at 83.7 and 87.4 eV correspond to the Au 4 $f_{7/2}$ and Au 4 $f_{5/2}$ for Au^0 species, respectively, indicating the successful loading of AuNPs on $BiVO_4$[52].

To evaluate the synergistic effect of plasmonic catalysis (AuNPs) and piezotronic effects ($BiVO_4$) on the catalytic performance of xAu/$BiVO_4$ heterostructures, we used the degradation of TC as a probe reaction to examine the catalytic activity under visible light irradiation, ultrasonic stimulation, and both ultrasonic and visible light irradiation, respectively [Figure 3]. As presented in Figure 3A, under sole ultrasonic stimulation, the TC degradation efficiency of the pure $BiVO_4$ is less than 28%. However, after modification with AuNPs, the degradation rate slightly increased, indicating that the charge induced by piezoelectric polarization of $BiVO_4$ crystals under ultrasonic vibration can be transferred to AuNPs to drive catalytic reactions[45]. In contrast, the photodegradation of TC was evaluated for all the samples under visible light [Figure 3B]. The decahedral $BiVO_4$ still exhibits low activity (~34%) within 60 min, which means that even under light excitation, the photocatalytic effect of pure $BiVO_4$ is limited. Additionally, the $BiVO_4$ samples were also synthesized with only exposed the pure (010) facets, (110) facets, and co-existing (010) and (110) facets for evaluating the influence of crystal facet effect on piezoelectric catalysis. As shown in Supplementary Figure 4

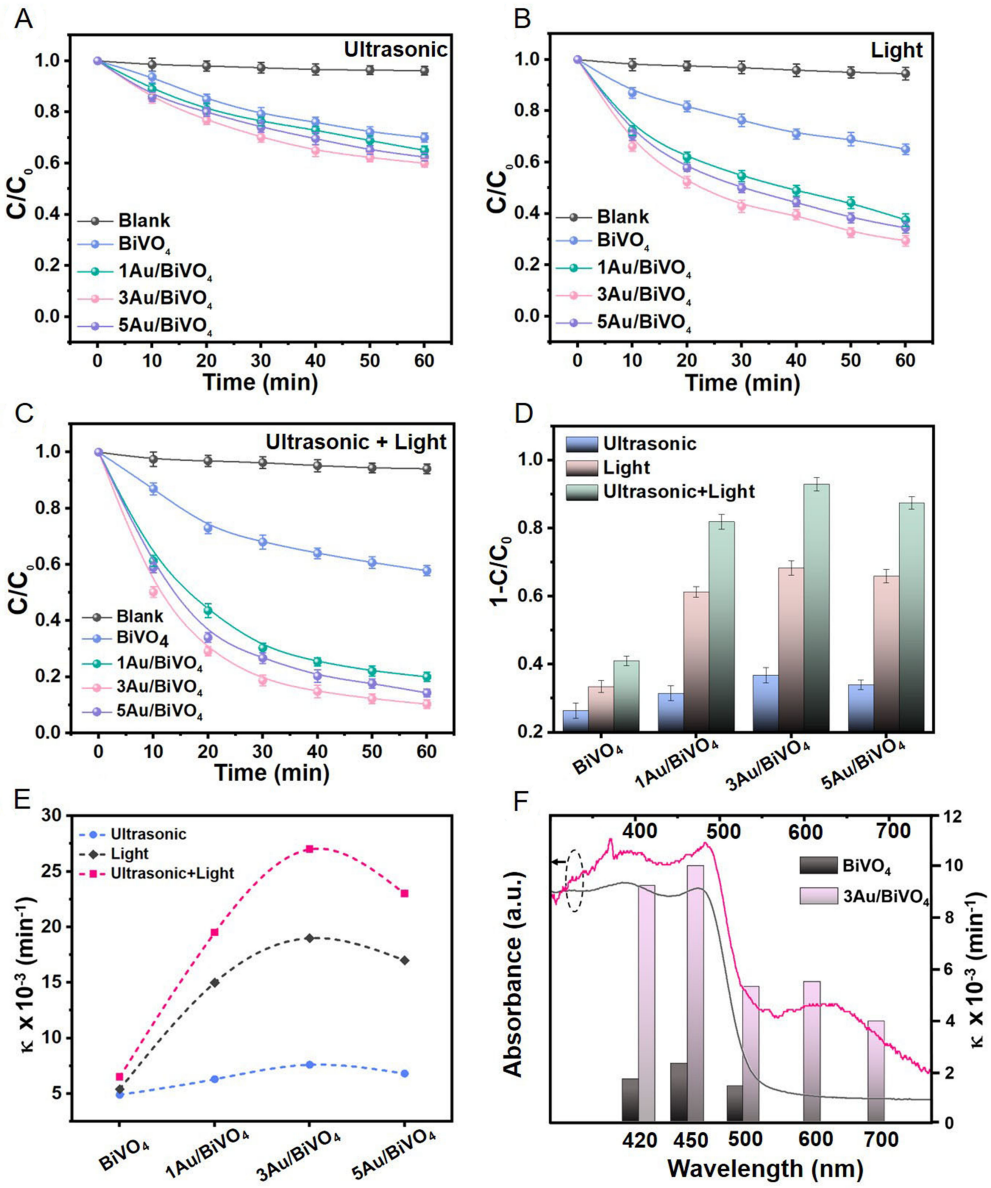

Figure 3. Catalytic degradation performance of TC over different samples. (A) Under ultrasonic stimulation; (B) Under visible light irradiation; (C) Catalytic degradation of TC under reaction conditions, both visible light and ultrasonic vibration; (D) The efficiency of ultrasound, photocatalysis, and both ultrasound and visible light irradiation in degrading TC for 60 min; (E) The rate constants *k* for TC degradation of $BiVO_4$ and x$Au/BiVO_4$; (F) The relationship between the degradation rate constant (*k*) of TC and absorption spectra of $BiVO_4$ and 3$Au/BiVO_4$ with different wavelengths. TC: Tetracycline; $BiVO_4$: bismuth vanadate.

, the decahedral $BiVO_4$ exhibits the optimal piezoelectric catalytic activity, indicating that the simultaneous presence of two facets is crucial to piezoelectric catalysis. This phenomenon is consistent with the research results of Ling *et al.*, where $SrTiO_3$ nanocrystals co-exposed to {001} and {110} facets exhibit the optimal piezoelectric catalytic activity for the degradation of RhB, compared to exposing only one facet[44]. Due to the formation of surface heterojunctions between the {001} and {110} facets, the positive and negative charges induced by piezoelectric polarization will migrate to the {001} and {110} facets, respectively, promoting charge transfer. Furthermore, the photocatalytic performance related to SPR is significantly improved after highly dispersed AuNPs. The 3$Au/BiVO_4$ showed a TC degradation efficiency of over 60%

within 60 min, which is due to the strong absorption of emitted light by AuNPs, inducing surface electron collective oscillation, generating hot electrons-holes pairs, and suppressing carrier recombination through the constructed heterostructure. Thus, the SPR effect and the heterostructure are key factors promoting the formation of $O_2^{\bullet-}$ and degradation of TC.

Notably, when ultrasound stimulation and visible light irradiation are used simultaneously in the catalytic process, all xAu/$BiVO_4$ heterostructures exhibit enhanced TC degradation activity. Impressively, the 3Au/$BiVO_4$ heterostructure achieved a degradation rate of TC exceeding 80% within 30 min and almost complete degradation within 60 min [Figure 3C]. Figure 3D shows a summary of TC degradation in all samples under the aforementioned catalytic conditions. The significant enhancement of catalytic performance of 3Au/$BiVO_4$ heterostructures under both light and ultrasound excitation is due to the synergistic coupling of piezoelectric and plasmonic effects. Due to the participation of ultrasonic vibration, piezoelectric polarization is effectively introduced into the $BiVO_4$ decahedron, and the induced built-in electric field helps to promote the separation and transmission of photogenerated charge carriers at the heterojunction interface, thereby more effectively promoting the generation of free radicals. A similar catalytic tendency towards the degradation of Rhodamine B (RhB) is observed [Supplementary Figure 5].

As shown in Supplementary Figure 6, we tested the piezoelectric photocatalytic performance of the catalyst at different TC concentrations (10-40 $mg{\cdot}L^{-1}$). The results showed that the degradation efficiency of 3Au/$BiVO_4$ piezoelectric photocatalyst for TC gradually decreased with increasing initial pollutant concentrations, with degradation efficiencies of 100%, 95%, 84%, and 70%, respectively. When the concentration of pollutants is too high, it will lead to an increase in the photogenerated electron-hole transport path. In addition, the intermediate products generated during the degradation process compete with TC, inhibiting photocatalytic activity. We further tested the piezoelectric catalytic degradation of TC by 3Au/$BiVO_4$ at different ultrasound powers and temperatures [Supplementary Figure 7].

In addition, we also analyzed the rate constant (k) of the samples under different catalytic conditions [Figure 3E]. The k value first increased with the increase of the Au mass ratio, and then the k value decreases as the loading amount continues to increase. This may be due to the insufficient generation of excited charge carriers by AuNPs with small loading amounts (such as 1Au/$BiVO_4$) for effective photocatalysis, while excessive Au loading (such as 5Au/$BiVO_4$) may lead to particle size increase, aggregation, poor SPR effect and may weaken the inhibition of holes-electrons recombination[36]. Therefore, an appropriate Au loading content (3Au/$BiVO_4$) is beneficial for enhancing photocatalytic performance. Furthermore, the wavelength-dependent photocatalytic performance experiments were employed. As presented in Figure 3F, for pure $BiVO_4$, the pseudo-first-order rate constant (k) of TC degradation decreases when irradiated with longer wavelengths greater than 550 nm, which is consistent with the trend of the optical absorption spectra of the $BiVO_4$ decahedron. Similarly, for 3Au/$BiVO_4$ samples, the TC degradation activity also follows the curve trajectory of the SPR resonance absorption peak. These results demonstrate that the plasmonic effect of AuNPs indeed plays a crucial role in the photocatalytic degradation of TC over xAu/$BiVO_4$ heterostructures. Importantly, it can be observed that there is no significant decrease in the photocatalytic activity of piezo-photocatalytic of tetracyclines after three cycles [Supplementary Figure 8]. Moreover, the SEM image after piezo-/photocatalytic reactions showed that AuNPs still exhibit high-density attachment on the surface of decahedral $BiVO_4$ after prolonged mechanical vibration treatment, proving the excellent stability of the 3Au/$BiVO_4$ sample [Supplementary Figure 9]. The Au/$BiVO_4$ catalyst was compared with other materials, and the results indicate that the 3Au/$BiVO_4$ has excellent performance in degrading TC [Supplementary Table 1].

To further explore the enhanced photocatalytic performance related to the SPR effect, single-particle PL spectroscopy was used to visualize fluorescence imaging of charge transfer behavior induced by SPR effect. Figure 4A and B shows the PL lifetime mapping of $BiVO_4$ and 3Au/$BiVO_4$. Further analyze the fluorescence spectrum information of $BiVO_4$ and fit the time-resolved PL (TRPL) spectra using a three-exponential function [Figure 4C]. The intensity-weighted average lifetime (τ_{av}) of entire $BiVO_4$ was 9.83 ns (the multi-exponential τ parameters are shown in Supplementary Table 2). Furthermore, the fitting τ_{av} of Point 1 on the (010) facet was 7.53 ns over $BiVO_4$ (the multi-exponential τ parameters are shown in Supplementary Table 3), and Point 2 on the (110) facet was 9.33 ns [Figure 4D]. The TPRL fitting results for different facets of particles are presented in Supplementary Figure 10. The PL emission center position of $BiVO_4$ is approximately 670 nm, and there is no significant spectral shift, which is consistent with our previous research on $BiVO_4$[46].

Previous studies have shown that plasmonic energy in metals is mainly transferred to semiconductors through three mechanisms: (i) light scattering; (ii) plasmonic-induced resonance energy transfer (PIRET); and (iii) hot electron injection[53]. In our system, it is not affected by light scattering (AuNPs > 50 nm)[54]. Direct electron transfer (DET) occurs after SPR excitation and subsequent decoherence, leaving behind a group of hot electrons that can transfer to the semiconductor[54,55]. In the case of modifying AuNPs, a uniformly quenched surface of PL was observed from PL lifetime mapping instead of regional PL bursts caused by multiple disordered modifications of AuNPs [Figure 4B], which suggests that the high-density uniform loading of AuNPs on the surface of $BiVO_4$. Compared with pure $BiVO_4$, the τ_{av} fitting results of 3Au/$BiVO_4$ particles was 7.25 ns (the multi-exponential τ parameters are shown in Supplementary Table 4), respectively, with a reduction factor of 26% [Figure 4D]. Additionally, the τ_{av} value for Point 1 was 4.75 ns (the multi-exponential τ parameters are shown in Supplementary Table 5); compared to $BiVO_4$, the τ_{av} decrease rate is ~37%. This phenomenon means that the injection of hot electrons induced by the SPR of AuNPs into $BiVO_4$ results in rapid charge recombination between some captured electrons in semiconductor $BiVO_4$ and holes in AuNPs, which then diffuses to the vicinity of AuNPs. Due to the radiative recombination process mediated by AuNPs occurring at the sub-picosecond level, it exhibits a shortened PL lifetime of 3Au/$BiVO_4$ particles.

Compared with pure $BiVO_4$, after loading AuNPs, the brightness of single-particle PL lifetime mapping weakens when PL quenching occurs [Figure 4A and B]. From Figure 4E and F, it can be observed that the decay rate of PL at the representative sites of 3Au/$BiVO_4$ particle is at least ~60%, compared to $BiVO_4$. This indicates that the 3Au/$BiVO_4$ heterostructure suppresses charge recombination. The PL emission in AuNPs comes from the direct excitation of hot electrons by SPR, which undergo radiation attenuation and lose energy, followed by the emission of photons. When AuNPs are loaded on $BiVO_4$, the hot electron transfer from AuNPs to $BiVO_4$ competes with radiation decay, forming a plasmonic induced electromagnetic field that effectively transfers electrons to the conduction band (CB) of $BiVO_4$. The plasmonic polaritons lead to the spatial separation of hot electron-hole pairs, which induces an effective charge separation. Additionally, the plasmonic-induced resonance energy can be non-radiatively transferred to the semiconductor through near-field dipole-dipole interactions, causing the charge carries in the semiconductor[54,56]. Moreover, the same trend was obtained from the other particles, confirming the reliability of our conclusion [Supplementary Figures 11 and 12]. In summary, plasmonic energy is transferred from AuNPs to $BiVO_4$, generating electron-hole pairs in semiconductors. Due to the lower laser intensity for AuNPs under the same testing conditions, the SPR emission generated by excitation is weaker. Therefore, the observed PL quenching in the Au/$BiVO_4$ system comes from the charge transfer dynamics on $BiVO_4$. In addition to the effective hot electron transfer, the enhancement of the local electric field at the Au/$BiVO_4$ interface can accelerate the excitation of $BiVO_4$. This may cause faster carrier complexation, leading to a decrease in the

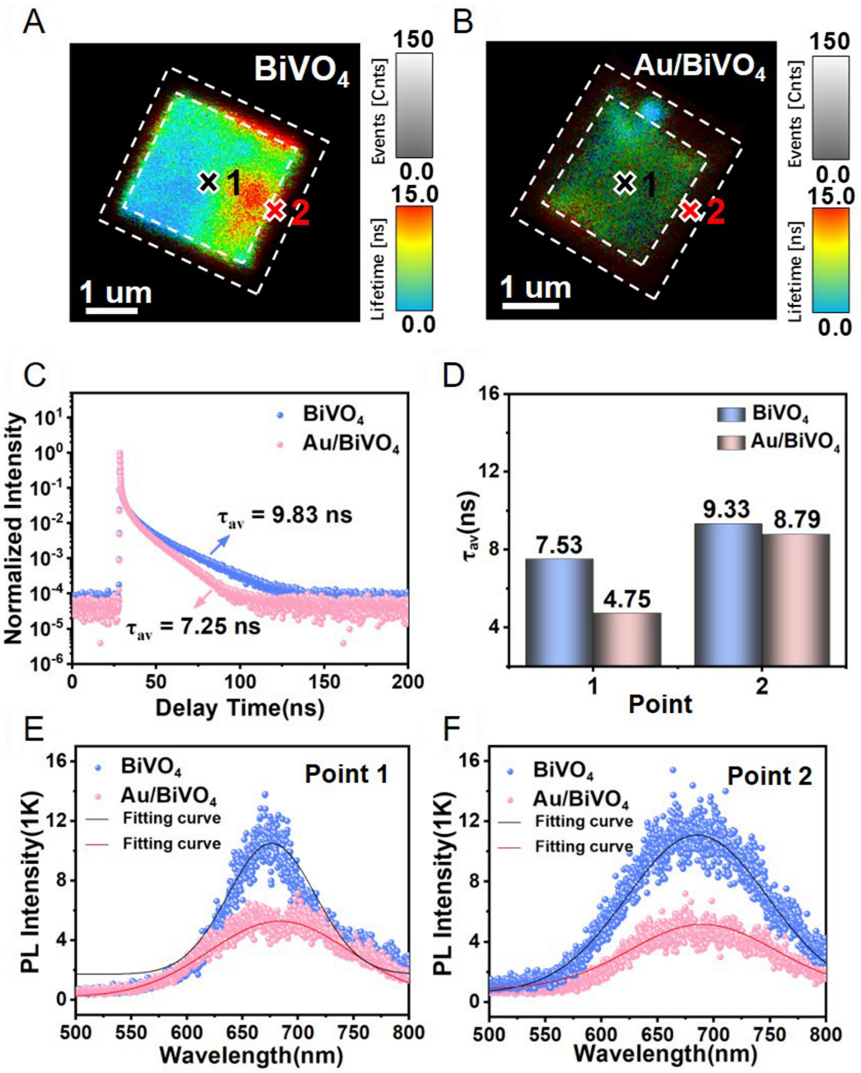

Figure 4. Single-particle PL spectroscopy measurements. PL lifetime mapping of (A) a single $BiVO_4$ particle and (B) a single $3Au/BiVO_4$ particle; (C) TRPL spectra of entire $BiVO_4$ and $3Au/BiVO_4$ particles; (D) The PL lifetime of different sites on single $BiVO_4$ and $3Au/BiVO_4$ particles; (E and F) The PL emission intensity spectra of different sites on single $BiVO_4$ and $3Au/BiVO_4$ particles. PL: Photoluminescence; $BiVO_4$: bismuth vanadate; TRPL: time-resolved PL.

PL lifetime, but the fast complexation rate does not represent an increase in the number of electron/hole pair complexes, and the decrease in the PL intensity suggests that the modification of the AuNPs promotes carrier migration. In addition, we conducted single-particle spectroscopic tests on $1Au/BiVO_4$. The obtained results are consistent with the activity of photocatalytic degradation of TC [Supplementary Figure 13].

Monitoring the charge transfer process during photocatalytic reactions is particularly important for understanding catalytic mechanisms. Figure 5A and B shows the PL lifetime mapping of individual $BiVO_4$ and $3Au/BiVO_4$ particles before and after addition to TC solution. After adding the TC solution, the τ_{av} decay rates of Point 1 and Point 2 over $BiVO_4$ were 25.3% and 23.1%, respectively [Figure 5C]. However, the τ_{av} decay rates of Point 1 and Point 2 over $3Au/BiVO_4$ were 18.5% and 11.4%, respectively [Figure 5D]. The PL lifetime decay rate of pure $BiVO_4$ is much higher than that of $3Au/BiVO_4$, suggesting that the photodegradation of TC promotes the carrier recombination of $BiVO_4$. This means that due to the weak

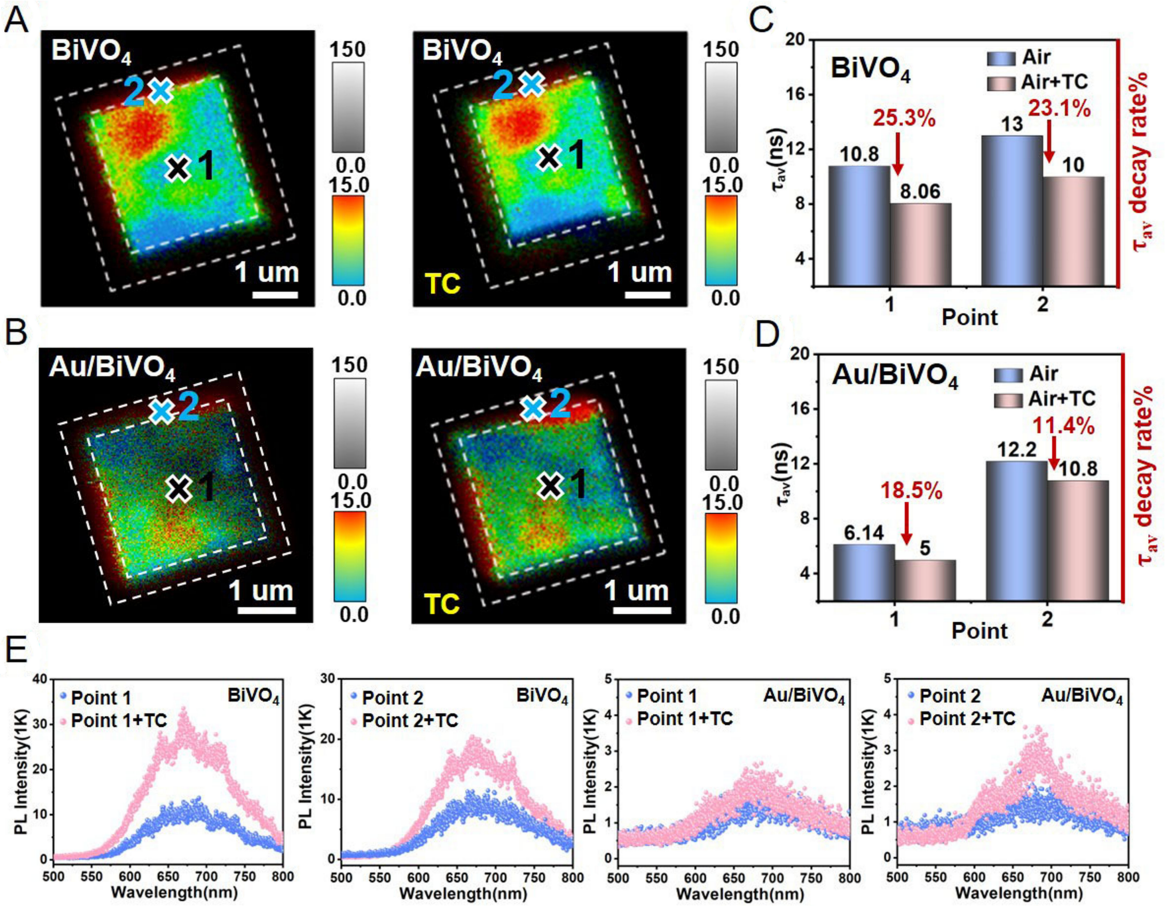

Figure 5. The PL lifetime mappings of single (A) $BiVO_4$ and (B) 3Au/$BiVO_4$ particle beforer and after adding TC solution to the reaction vessel; The τ_{av} with decay rate on representative points of (C) $BiVO_4$ and (D) 3Au/$BiVO_4$ particle in air and after adding TC solution; (E) PL intensity of Point 1 and Point 2 over $BiVO_4$ and 3Au/$BiVO_4$ particle before after adding TC solution. PL: Photoluminescence; $BiVO_4$: bismuth vanadate; TC: tetracycline.

mobility of electron-hole pairs in $BiVO_4$, the degradation of TC leads to a decrease in charge carriers, resulting in a significant reduction in PL lifetime. However, the PL lifetime of 3Au/$BiVO_4$ only slightly decreased, indicating an effective transfer of plasmonic energy from AuNPs to $BiVO_4$, which increased the production of hot electrons and induced electron-hole pairs. As shown in Figure 5E, the PL emission of $BiVO_4$ significantly increases, which may be due to the promotion of carrier recombination by the addition of TC. The effect of TC on the PL emission of 3Au/$BiVO_4$ heterostructures is relatively weak, indicating that the modification of AuNPs enhances the photocatalytic degradation of TC, and the injected electrons move to the active site of $BiVO_4$ to participate in the catalytic reaction.

In order to further understand the charge transfer and separation ability on the catalyst, the photoelectric performance of $BiVO_4$ and Au/$BiVO_4$ catalysts was tested. The xAu/$BiVO_4$ exhibited higher photocurrent density than $BiVO_4$, with 3Au/$BiVO_4$ exhibiting the highest photocurrent density under full spectrum light irradiation [Figure 6A]. As is well known, a smaller curvature radius indicates better separation ability of electron-hole pairs [Figure 6B]. The 3Au/$BiVO_4$ has the smallest curvature radius, indicating that charge carriers can be quickly transported to the reaction site. This indicates that the 3Au/$BiVO_4$ heterostructure has superior electron separation and transfer performance, which is consistent with the single-particle PL spectra and tested photocatalytic performance.

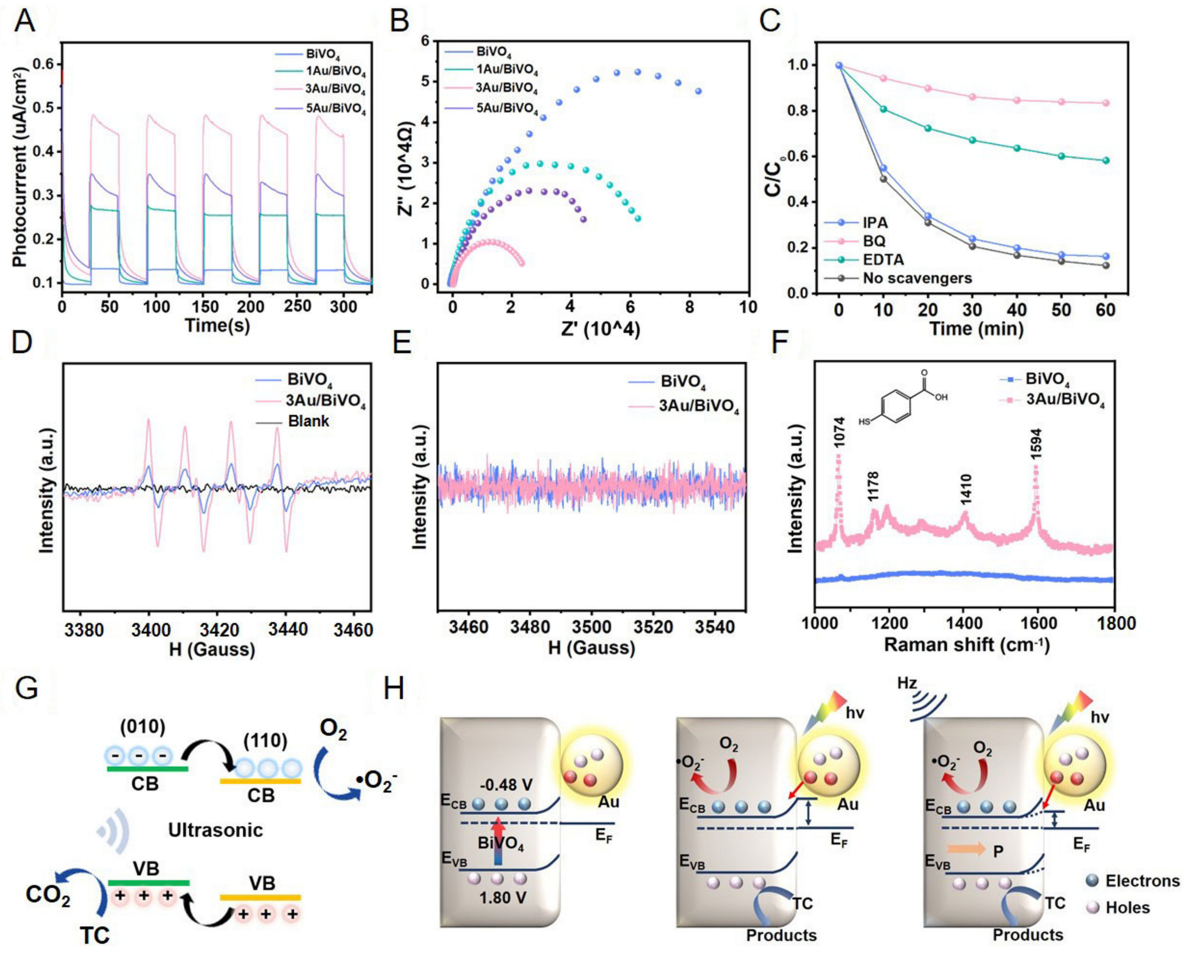

Figure 6. (A) The transient photocurrent response curves of $BiVO_4$ and Au/$BiVO_4$ catalysts; (B) EIS plots of $BiVO_4$ and Au/$BiVO_4$ catalysts; (C) Active species capture experiments in piezo-photocatalytic processes; ESR spectra of (D) DMPO-$O_2^{\bullet-}$ and (E) DMPO-•OH; (F) Surface enhanced Raman scattering testing of 4-MBA on the $BiVO_4$ and 3Au/$BiVO_4$ heterostructure; (G) Schematic illustration for (010) and (110) surface heterojunction; (H) Schematic diagram of piezo-/photocatalytic mechanism. $BiVO_4$: Bismuth vanadate; EIS: electrochemical impedance spectroscopy; ESR: electron spin resonanc; DMPO: 5,5-dimethyl-1-pyrroline N-oxide; 4-MBA: 4-mercaptobenzoic acid.

Verify the main active species in the piezoelectric photocatalytic process through free radical capture experiments. Where ethanol, benzoquinone (BQ) and isopropyl alcohol (IPA) were used as scavengers for capturing h^+, $O_2^{\bullet-}$ and •OH, respectively. As presented in Figure 6C, there was no significant change in the degradation rate of TC after adding IPA in the reaction conditions of both visible light and ultrasonic vibration, while the degradation rate of TC was significantly inhibited by the addition of BQ, proving that $O_2^{\bullet-}$ is the main reactive species for TC degradation. When the h^+ is captured, the degradation rate of TC also decreases, indicating that the h^+ also participates in the reaction as an active species. Moreover, 5,5-dimethyl-1-pyrroline N-oxide (DMPO) was used as the capture reagent and further conducted the electron spin resonance (ESR) spin-trap experiments to identify the free radicals ($O_2^{\bullet-}$ and •OH)[57,58]. As presented in Figure 6D and E, only EPR signals belonging to DMPO-$O_2^{\bullet-}$ were detected, with no signal belonging to the •OH radical. Moreover, the signal intensity of $O_2^{\bullet-}$ in the 3Au/$BiVO_4$ samples is significantly higher than that of $BiVO_4$, indicating that the loading of AuNPs promotes the improvement of photocatalytic performance.

Surface enhanced Raman scattering (SERS) was used to verify the existence of SPR effect [Figure 6F]. Raman spectra were measured using 4-mercaptobenzoic acid (4-MBA) as a probe molecule under 633 nm laser excitation. The characteristic peaks located at 1,074 and 1,594 cm^{-1} belong to the vibration mode of $\nu_{8\alpha}$ aromatic ring and the breathing mode of $\nu_{12\alpha}$ ring, respectively. The two peaks at 1,410 and 1,178 cm^{-1} are attributed to the stretching mode of $\nu_{(COO-)}$ and deformation mode of C-H, respectively[36]. For the 3Au/$BiVO_4$ hybrid structure, characteristic peaks corresponding to 4-MBA can be clearly observed, but these peaks were not detected in the original $BiVO_4$ sample. The performance of a highly sensitive SERS probe for 4-MBA based on 3Au/$BiVO_4$ heterostructure indicates strong plasmonic effect and strong electromagnetic field generated by AuNPs attached to the surface of the $BiVO_4$.

In order to further investigate the charge separation process caused by piezoelectric polarization under ultrasonic vibration, we simulated this piezoelectric process by applying an electric field to $BiVO_4$ for polarization treatment and used single-particle spectroscopy for *in situ* monitoring. During the polarization process, the strong electric field applied to the material causes the arrangement of grain domains to become more orderly. After removing the electric field, due to the pinning effect caused by microscopic defects in the lattice, most dipoles will not return to their initial orientation. In this way, we obtained a material composed of a large number of micro-dipoles with roughly the same orientation. Supplementary Figures 14-16 show the PL lifetime mapping of $BiVO_4$ and 3Au/$BiVO_4$ particles before and after polarization treatment, along with the fitting of τ_{av} for the overall particles, representative sites, and different facets. The results showed that both $BiVO_4$ and 3Au/$BiVO_4$ particles showed a trend of increasing PL lifetime after polarization treatment, but the PL lifetime increase rate of 3Au/$BiVO_4$ was higher than that of pure $BiVO_4$. Similarly, we also conducted in situ testing of the changes in PL emission intensity before and after polarization [Supplementary Figures 16-18]. Four representative sites were selected for each particle, and the PL decay rates at the sites of $BiVO_4$ particles were 14%, 25%, 15%, and 16%, respectively, while 3Au/$BiVO_4$ corresponded to 36%, 30%, 37%, and 39%. The above results indicate that the piezoelectric effect indeed promotes the separation of charge carriers, and the AuNPs on the surface of $BiVO_4$ may serve as electron capture sites, further suppressing recombination of electron-hole pairs. To further demonstrate the piezoelectric/ferroelectric performance of 3Au/$BiVO_4$, piezoresponse force microscopy (PFM) was further used to detect its piezoelectric response signal. As shown in Supplementary Figure 19, under a voltage bias of -10 V, the phase angle of the $BiVO_4$ decahedron undergoes a phase transition of approximately 180°, indicating a local transition in the direction of ferroelectric polarization in 3Au/$BiVO_4$. In addition, the butterfly-shaped hysteresis loop of the amplitude confirms its piezoelectric/ferroelectric properties.

In our system, due to the higher potential of $O_2/O_2^{\bullet-}$ (-0.33 eV) compared to the CB of $BiVO_4$ (-0.48 eV) [Supplementary Figure 20], these electrons are subsequently captured and reduced to $O_2^{\bullet-}$ by dissolved O_2 molecules[46]. Meanwhile, due to the SPR effect, the collective oscillation of electrons on the AuNP surface will generate a built-in electric field and high-energy hot electrons, which will accelerate the separation of photogenerated electrons and holes, thereby improving photocatalytic activity. In addition, the h^+ generated in the valence band (VB) also promotes the degradation of TC. This is also consistent with the results of the ESR and capture tests mentioned before. To explore the intermediate products of piezo-photocatalytic degradation of TC in 3Au/$BiVO_4$ composite materials, the composition of the reaction solution at different reaction times was investigated by high-performance liquid chromatography-mass spectrometry (HPLC-MS) spectroscopy. Based on the analysis results and previous research, the degradation products and pathways of TC were speculated, and four possible pathways during the reaction process were proposed [Figure 7].

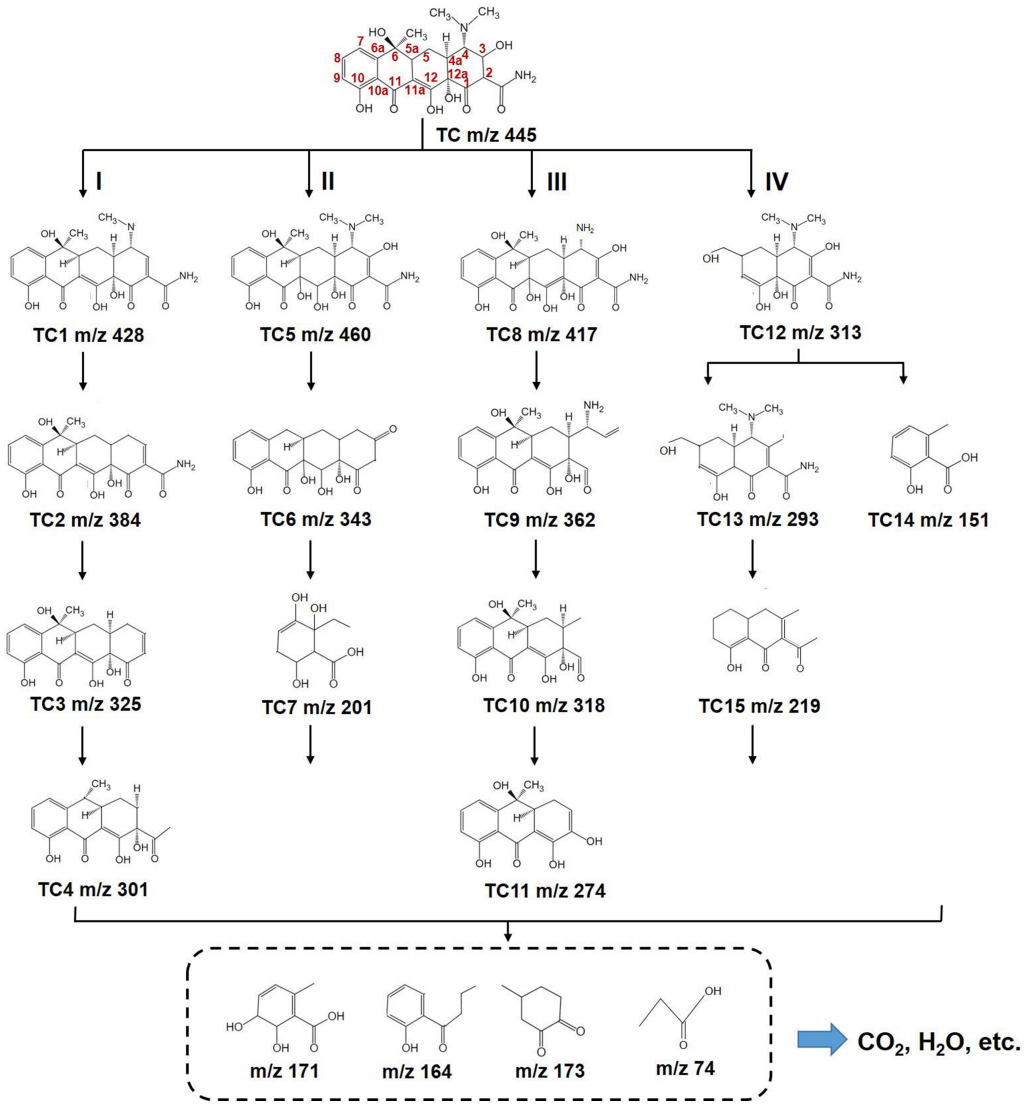

Figure 7. TC degradation pathways for 3Au/$BiVO_4$ under visible light and ultrasonic vibrations. TC: Tetracycline; $BiVO_4$: bismuth vanadate.

In pathway I, the formation of TC1 (m/z = 428) may originate from the dehydroxylation process in TC, while TC2 (m/z = 384) is generated by the cleavage of C-N bonds. In addition, TC3 (m/z = 325) and TC4 (m/z = 301) are caused by reactions between molecules and active intermediates, leading to deprotonation of hydroxyl groups and subsequent decarboxylation. For pathway II, the double bonds on C11a-C12 have a higher electron density than those on C2-C3, making them more susceptible to attack and producing TC5 (m/z = 460). The mixture of TC6 (m/z = 343) may be due to the continuous deamination and methylation in TC5. As the irradiation time prolongs, TC6 undergoes additional ring dissociation, forming TC7 (m/z = 201). For pathway III, due to the decrease in energy of C–C and C–N bonds, TC undergoes a dealkylation reaction to generate TC8 (m/z = 417). Subsequently, TC8 loses acyl and hydroxyl groups, generating TC9 (m/z = 362). As the reaction time prolongs, TC9 undergoes an open-loop process, generating TC10 (m/z = 318). In addition, due to the destruction of the carbon ring, TC10 undergoes dehydroxylation, resulting in the formation of TC11 (m/z = 274). As shown in degradation pathway IV, the C-ring of the TC molecule is directly attacked and cleaved into two products (m/z = 313, 151). As shown in

Supplementary Figure 21, degradation pathway IV is the main reason for the decrease in the 370 nm peak in the spectrum. As the reaction continues, these unstable intermediates are further oxidized into low molecular organic molecules. Finally, organic molecules are further mineralized into small inorganic substances such as carbon dioxide, water, and other products.

Based on the above results and analysis, we constructed an energy level diagram to describe the charge transport mechanism in 3Au/$BiVO_4$ piezo-photocatalysts. Based on the energy bandgap and Mott Schottky (M-S) curve, the conduction and VB positions of $BiVO_4$ were calculated to be -0.48V and 1.88 V [*vs.* normal hydrogen electrode (NHE)], allowing for the generation of $O_2^{\bullet-}$. Importantly, experiments have shown that $BiVO_4$ decahedra with co-exposed (010) and (110) facets exhibit optimal piezoelectric catalytic performance, and this piezoelectric polarization based on crystal facet effect further enhances the carrier separation ability [Figure 6G]. As presented in Figure 6H, when the 3Au/$BiVO_4$ catalyst was irradiated by visible light, the high-energy hot electrons induced by plasma resonance in AuNPs will overcome the Schottky barrier and be injected into the CB of $BiVO_4$. In addition, when the $BiVO_4$ is exposed to ultrasonic vibration, an internal electric field induced by piezoelectric polarization is generated inside the $BiVO_4$. The internal piezoelectric field causes the energy band near the Au/$BiVO_4$ interface to bend, resulting in a decrease in the Schottky barrier and an increase in the injection efficiency of hot electrons from AuNPs to $BiVO_4$. Therefore, the key to the significantly enhanced catalytic activity of Au/$BiVO_4$ heterostructures lies in the synergistic coupling of the plasmonic effect of AuNPs and the charge separation generated by the piezoelectric polarization of $BiVO_4$ under ultrasound stimulation.

CONCLUSIONS

In summary, x Au/$BiVO_4$ (x = 0, 1, 3 and 5) plasmonic photocatalysts were prepared and their piezo-photocatalytic activity was explored. Ultrasonic stimulation generates piezoelectric polarization in the decahedral $BiVO_4$; under the combined action of light irradiation and piezoelectric effect, the SPR induced high-energy hot electrons are transferred to the surface of $BiVO_4$, effectively promoting the separation of charge carriers. Under piezoelectric assistance, the 3Au/$BiVO_4$ heterostructure significantly improved the photocatalytic degradation rate of TC and RhB (degrading 95% of TC within 60 min). The electron-hole pair transport and recombination processes induced by plasmonic and piezoelectric polarization in 3Au/$BiVO_4$ heterojunctions were monitored using single-particle PL spectroscopy. This study contributes to the promotion and design of other plasmonic/piezoelectric catalytic systems and has broad application prospects in pollution control.

DECLARATIONS

Authors' contributions

Made significant contributions to the conception and design of the research, performed data analysis and interpretation, and wrote the draft of the manuscript: Zhang Y

Provided administrative, technical, and material support: Zheng Z

Discussed and revised the manuscript: Liu Y, Gong X, Wang Z, Liu Y, Wang P, Cheng H, Huang B, Zheng Z

Availability of data and materials

The data supporting this article have been included as part of the Supplementary Materials.

Financial support and sponsorship

This work was supported by the National Natural Science Foundation of China (Nos. 22222202, 22072072), the National Key Research and Development Program of China (No. 2020YFA0710301), the Natural

Science Foundation of Shandong Province (No. ZR2021JQ06), the Shandong University multidisciplinary research and innovation team of young scholars (Nos. 2020QNQT11, 2020QNQT012), and the Qilu Young Scholars and Outstanding Young Scholars Projects of Shandong University.

Conflicts of interest

All authors declared that there are no conflicts of interest.

Ethical approval and consent to participate

Not applicable.

Consent for publication

Not applicable.

Copyright

REFERENCES

1. Li S, Shi W, Liu W, et al. A duodecennial national synthesis of antibiotics in China's major rivers and seas (2005-2016). *Sci Total Environ* 2018;615:906-17. DOI PubMed
2. Rodriguez-Narvaez OM, Peralta-Hernandez JM, Goonetilleke A, Bandala ER. Treatment technologies for emerging contaminants in water: a review. *Chem Eng J* 2017;323:361-80. DOI
3. Li S, Hu J. Photolytic and photocatalytic degradation of tetracycline: effect of humic acid on degradation kinetics and mechanisms. *J Hazard Mater* 2016;318:134-44. DOI PubMed
4. Reheman A, Kadeer K, Okitsu K, et al. Facile photo-ultrasonic assisted reduction for preparation of rGO/Ag_2CO_3 nanocomposites with enhanced photocatalytic oxidation activity for tetracycline. *Ultrason Sonochem* 2019;51:166-77. DOI
5. Cheng Z, Ling L, Wu Z, Fang J, Westerhoff P, Shang C. Novel visible light-driven photocatalytic chlorine activation process for carbamazepine degradation in drinking water. *Environ Sci Technol* 2020;54:11584-93. DOI
6. Chiu Y, Chang T, Chen C, Sone M, Hsu Y. Mechanistic insights into photodegradation of organic dyes using heterostructure photocatalysts. *Catalysts* 2019;9:430. DOI
7. Shen J, Li Y, Zhao H, et al. Modulating the photoelectrons of g-C_3N_4 via coupling $MgTi_2O_5$ as appropriate platform for visible-light-driven photocatalytic solar energy conversion. *Nano Res* 2019;12:1931-6. DOI
8. Ye S, Yan M, Tan X, et al. Facile assembled biochar-based nanocomposite with improved graphitization for efficient photocatalytic activity driven by visible light. *Appl Catal B Environ* 2019;250:78-88. DOI
9. Deng Y, Zhou Z, Zeng H, et al. Phosphorus and kalium co-doped g-C_3N_4 with multiple-locus synergies to degrade atrazine: Insights into the depth analysis of the generation and role of singlet oxygen. *Appl Catal B Environ* 2023;320:121942. DOI
10. Chen L, Maigbay MA, Li M, Qiu X. Synthesis and modification strategies of g-C_3N_4 nanosheets for photocatalytic applications. *Adv Powder Mater* 2024;3:100150. DOI
11. Liu T, Zhang D, Yin K, Yang C, Luo S, Crittenden JC. Degradation of thiacloprid via unactivated peroxymonosulfate: the overlooked singlet oxygen oxidation. *Chem Eng J* 2020;388:124264. DOI
12. Wang K, Xing Z, Meng D, et al. Hollow $MoSe_2$@Bi_2S_3/CdS core-shell nanostructure as dual Z-scheme heterojunctions with enhanced full spectrum photocatalytic-photothermal performance. *Appl Catal B Environ* 2021;281:119482. DOI
13. Zhang L, Wang J, Wang H, et al. Rational design of smart adsorbent equipped with a sensitive indicator via ligand exchange: a hierarchical porous mixed-ligand MOF for simultaneous removal and detection of Hg^{2+}. *Nano Res* 2021;14:1523-32. DOI
14. Yang M, Tan CF, Lu W, Zeng K, Ho GW. Spectrum tailored defective 2D semiconductor nanosheets aerogel for full-spectrum-driven photothermal water evaporation and photochemical degradation. *Adv Funct Mater* 2020;30:2004460. DOI
15. Chen R, Zhang H, Dong Y, Shi H. Dual metal ions/BNQDs boost PMS activation over copper tungstate photocatalyst for antibiotic removal: intermediate, toxicity assessment and mechanism. *J Mater Sci Technol* 2024;170:11-24. DOI
16. Han T, Shi H, Chen Y. Facet-dependent CuO/{010}$BiVO_4$ S-scheme photocatalyst enhanced peroxymonosulfate activation for efficient norfloxacin removal. *J Mater Sci Technol* 2024;174:30-43. DOI
17. Li H, Sang Y, Chang S, et al. Enhanced ferroelectric-nanocrystal-based hybrid photocatalysis by ultrasonic-wave-generated piezophototronic effect. *Nano Lett* 2015;15:2372-9. DOI
18. Sun C, Fu Y, Wang Q, Xing L, Liu B, Xue X. Ultrafast piezo-photocatalytic degradation of organic pollutions by Ag_2O/tetrapod-ZnO nanostructures under ultrasonic/UV exposure. *RSC Adv* 2016;6:87446-53. DOI
19. Huang H, Tu S, Du X, Zhang Y. Ferroelectric spontaneous polarization steering charge carriers migration for promoting photocatalysis and molecular oxygen activation. *J Colloid Interface Sci* 2018;509:113-22. DOI PubMed

20. Tang R, Gong D, Zhou Y, et al. Unique g-C_3N_4/PDI-g-C_3N_4 homojunction with synergistic piezo-photocatalytic effect for aquatic contaminant control and H_2O_2 generation under visible light. *Appl Catal B Environ* 2022;303:120929. DOI
21. Tang R, Zeng H, Feng C, et al. Twisty C-TiO_2/PCN S-scheme heterojunction with enhanced n→π* electronic excitation for promoted piezo-photocatalytic effect. *Small* 2023;19:e2207636. DOI PubMed
22. Wang ZL, Song J. Piezoelectric nanogenerators based on zinc oxide nanowire arrays. *Science* 2006;312:242-6. DOI PubMed
23. Wang ZL. Piezotronic and piezophototronic effects. *J Phys Chem Lett* 2010;1:1388-93. DOI
24. Chen X, Xu S, Yao N, Shi Y. 1.6 V nanogenerator for mechanical energy harvesting using PZT nanofibers. *Nano Lett* 2010;10:2133-7. DOI PubMed
25. Hu Y, Zhang Y, Xu C, Lin L, Snyder RL, Wang ZL. Self-powered system with wireless data transmission. *Nano Lett* 2011;11:2572-7. DOI
26. Starr MB, Shi J, Wang X. Piezopotential-driven redox reactions at the surface of piezoelectric materials. *Angew Chem Int Ed Engl* 2012;51:5962-6. DOI PubMed
27. Tan CF, Ong WL, Ho GW. Self-biased hybrid piezoelectric-photoelectrochemical cell with photocatalytic functionalities. *ACS Nano* 2015;9:7661-70. DOI PubMed
28. Li S, Zhao Z, Zhao J, Zhang Z, Li X, Zhang J. Recent advances of ferro-, piezo-, and pyroelectric nanomaterials for catalytic applications. *ACS Appl Nano Mater* 2020;3:1063-79. DOI
29. Li S, Zhao Z, Yu D, et al. Few-layer transition metal dichalcogenides (MoS_2, WS_2, and WSe_2) for water splitting and degradation of organic pollutants: understanding the piezocatalytic effect. *Nano Energy* 2019;66:104083. DOI
30. Zhang X, Chen YL, Liu RS, Tsai DP. Plasmonic photocatalysis. *Rep Prog Phys* 2013;76:046401. DOI PubMed
31. Linic S, Christopher P, Ingram DB. Plasmonic-metal nanostructures for efficient conversion of solar to chemical energy. *Nat Mater* 2011;10:911-21. DOI PubMed
32. Tong F, Liang X, Wang Z, et al. Probing the mechanism of plasmon-enhanced ammonia borane methanolysis on a CuAg alloy at a single-particle level. *ACS Catal* 2021;11:10814-23. DOI
33. Zheng Z, Tachikawa T, Majima T. Single-particle study of Pt-modified Au nanorods for plasmon-enhanced hydrogen generation in visible to near-infrared region. *J Am Chem Soc* 2014;136:6870-3. DOI PubMed
34. Fei J, Li J. Controlled preparation of porous TiO_2-Ag nanostructures through supramolecular assembly for plasmon-enhanced photocatalysis. *Adv Mater* 2015;27:314-9. DOI PubMed
35. Li S, Zhang J, Kibria MG, et al. Remarkably enhanced photocatalytic activity of laser ablated Au nanoparticle decorated $BiFeO_3$ nanowires under visible-light. *Chem Commun* 2013;49:5856-8. DOI PubMed
36. Xu S, Guo L, Sun Q, Wang ZL. Piezotronic effect enhanced plasmonic photocatalysis by AuNPs/$BaTiO_3$ heterostructures. *Adv Funct Mater* 2019;29:1808737. DOI
37. Li S, Zhao Z, Liu M, et al. Remarkably enhanced photocatalytic performance of Au/$AgNbO_3$ heterostructures by coupling piezotronic with plasmonic effects. *Nano Energy* 2022;95:107031. DOI
38. Xu J, Zhang Q, Gao X, et al. Highly efficient Fe^{III} -initiated self-cycled fenton system in piezo-catalytic process for organic pollutants degradation. *Angew Chem Int Ed Engl* 2023;135:e202307018. DOI PubMed
39. Chen F, Huang H, Ye L, et al. Thickness-dependent facet junction control of layered $BiOIO_3$ Single crystals for highly efficient CO_2 photoreduction. *Adv Funct Mater* 2018;28:1804284. DOI
40. Zhou FQ, Fan JC, Xu QJ, Min YL. $BiVO_4$ nanowires decorated with CdS nanoparticles as Z-scheme photocatalyst with enhanced H_2 generation. *Appl Catal B Environ* 2017;201:77-83. DOI
41. Kim TW, Choi KS. Nanoporous $BiVO_4$ photoanodes with dual-layer oxygen evolution catalysts for solar water splitting. *Science* 2014;343:990-4. DOI PubMed
42. Zhang B, Wang L, Zhang Y, Ding Y, Bi Y. Ultrathin FeOOH nanolayers with abundant oxygen vacancies on $BiVO_4$ photoanodes for efficient water oxidation. *Angew Chem Int Ed Engl* 2018;57:2248-52. DOI PubMed
43. Li R, Zhang F, Wang D, et al. Spatial separation of photogenerated electrons and holes among {010} and {110} crystal facets of $BiVO_4$. *Nat Commun* 2013;4:1432. DOI PubMed
44. Ling J, Wang K, Wang Z, Huang H, Zhang G. Enhanced piezoelectric-induced catalysis of $SrTiO_3$ nanocrystal with well-defined facets under ultrasonic vibration. *Ultrason Sonochem* 2020;61:104819. DOI PubMed
45. Wei Y, Zhang Y, Geng W, Su H, Long M. Efficient bifunctional piezocatalysis of Au/$BiVO_4$ for simultaneous removal of 4-chlorophenol and Cr(VI) in water. *Appl Catal B Environ* 2019;259:118084. DOI
46. Zhang Y, Liu Y, Zhang T, et al. In situ monitoring of the spatial distribution of oxygen vacancies and enhanced photocatalytic performance at the single-particle level. *Nano Lett* 2023;23:1244-51. DOI PubMed
47. Anwer S, Bharath G, Iqbal S, et al. Synthesis of edge-site selectively deposited Au nanocrystals on TiO_2 nanosheets: an efficient heterogeneous catalyst with enhanced visible-light photoactivity. *Electrochim Acta* 2018;283:1095-104. DOI
48. Zhang J, Lu Y, Ge L, et al. Novel AuPd bimetallic alloy decorated 2D $BiVO_4$ nanosheets with enhanced photocatalytic performance under visible light irradiation. *Appl Catal B Environ* 2017;204:385-93. DOI
49. Wang S, He T, Chen P, et al. In situ formation of oxygen vacancies achieving near-complete charge separation in planar $BiVO_4$ photoanodes. *Adv Mater* 2020;32:e2001385. DOI PubMed
50. Li H, Sun Y, Cai B, et al. Hierarchically Z-scheme photocatalyst of Ag@AgCl decorated on $BiVO_4$ (040) with enhancing photoelectrochemical and photocatalytic performance. *Appl Catal B Environ* 2015;170-1:206-14. DOI

51. Gu S, Li W, Wang F, Wang S, Zhou H, Li H. Synthesis of buckhorn-like $BiVO_4$ with a shell of CeO*x* nanodots: effect of heterojunction structure on the enhancement of photocatalytic activity. *Appl Catal B Environ* 2015;170-1:186-94. DOI
52. Van CN, Chang WS, Chen JW, et al. Heteroepitaxial approach to explore charge dynamics across Au/$BiVO_4$ interface for photoactivity enhancement. *Nano Energy* 2015;15:625-33. DOI
53. Wu N. Plasmonic metal-semiconductor photocatalysts and photoelectrochemical cells: a review. *Nanoscale* 2018;10:2679-96. DOI
54. Tian Y, Tatsuma T. Plasmon-induced photoelectrochemistry at metal nanoparticles supported on nanoporous TiO_2. *Chem Commun* 2004:1810-1. DOI PubMed
55. Tian Y, Tatsuma T. Mechanisms and applications of plasmon-induced charge separation at TiO_2 films loaded with gold nanoparticles. *J Am Chem Soc* 2005;127:7632-7. DOI PubMed
56. Cushing SK, Li J, Meng F, et al. Photocatalytic activity enhanced by plasmonic resonant energy transfer from metal to semiconductor. *J Am Chem Soc* 2012;134:15033-41. DOI
57. Ding X, Zhao K, Zhang L. Enhanced photocatalytic removal of sodium pentachlorophenate with self-doped Bi_2WO_6 under visible light by generating more superoxide ions. *Environ Sci Technol* 2014;48:5823-31. DOI PubMed
58. Huang H, Li X, Wang J, et al. Anionic group self-doping as a promising strategy: band-gap engineering and multi-functional applications of high-performance CO_3^{2-} -Doped $Bi_2O_2CO_3$. *ACS Catal* 2015;5:4094-103. DOI